JTTEE5 14:362-368
DOI: 10.1361/105996305X59431
1059-9630/$19.00 © ASM International

Peer Reviewed

Microstructure of Vacuum Plasma-Sprayed Boron Carbide

H.R. Salimijazi, T.W. Coyle, J. Mostaghimi, and L. Leblanc

(Submitted December 2, 2003; in revised form June 14, 2004)

In the present study, boron carbide was deposited on Ti-6%Al-4%V alloy by vacuum plasma spraying. Chemical and phase compositions of the initial starting powder and the as-sprayed deposit were characterized using hot gas extraction, x-ray photoelectron spectroscopy, Raman spectroscopy, x-ray diffraction, and transmission electron microscopy. Mechanical properties of the deposition were assessed by microhardness and nanohardness indentation. The microstructure consisted of equiaxed boron carbide grains, microcrystalline particles, and amorphous carbon regions. The amount of boron oxide and amorphous carbon in the coating was increased compared with the initial powder. The measured microhardness was slightly higher than values reported previously (1033 ± 200 HV). There was significant variation in measured nanohardness (−100 + 39 GPa) from point to point caused by multiple phases, splat boundaries, and porosity in the deposited structure. Carbon segregation to grain boundaries and/or splat boundaries in boron carbide was observed directly using spatially resolved electron energy loss spectroscopy method.

Keywords B_4C decomposition, B_4C microstructure, boron carbide characterization, boron depletion, chemical and phase composition, micro- and nanohardness, vacuum plasma spraying

1. Introduction

Boron carbide (B_4C) is the third hardest material after diamond and boron nitride at room temperature, and its hardness is retained to high temperatures (Ref 1). It has a high resistance to wear and thermal shock. Two well-known applications of B_4C, which take advantage of these attractive properties, are as an abrasive and for lightweight armor. This material has also received attention for application in nuclear fusion reactors because the low atomic numbers of boron and carbon result in low x-ray absorption, and exposure to neutron irradiation does not cause radioactive decay (Ref 2-5).

Dense, single-phase B_4C material is difficult to produce using powder metallurgy techniques Although dense material can be produced using chemical vapor deposition and physical vapor deposition techniques (Ref 1), the deposition of thick sections is time consuming and expensive. Work on the deposition of B_4C by both atmospheric plasma spraying (APS) and vacuum plasma spraying (VPS) has been reported (Ref 2-6). However, the deposition of dense coatings is difficult because of the high vapor pressure at elevated temperatures and the high melting point of B_4C.

Layered deposition of B_4C and titanium alloy by VPS would be attractive for lightweight ballistic protection applications if B_4C with sufficiently high values of hardness and elastic modulus could be produced. The work reported here was undertaken to assess the progress made in optimizing deposition conditions for the production of B_4C for armor applications by identifying the factors limiting the hardness. Microhardness and nanohardness measurements of the as-sprayed material were performed, and the microstructure and chemical and phase compositions of the as-sprayed structure were investigated.

H.R. Salimijazi, T.W. Coyle, and **J. Mostaghimi,** Centre for Advanced Coatings Technologies, University of Toronto, Toronto, Ontario, Canada; and **L. Leblanc,** formerly with PyroGenesis, Inc., Montreal, Quebec, Canada. Contact e-mail: mostag@mie.utoronto.ca.

2. Experimental Procedures

The specimens were made by deposition of B_4C on Ti-6Al-4V alloy substrate using a VPS process developed by PyroGenesis, Inc., Montreal, Canada. An F4VB gun from Plasma-Technik, Switzerland, was used in a low-pressure controlled atmosphere chamber. Commercially prepared B_4C powder was used as the feedstock. The VPS procedure and spray conditions have been described elsewhere (Ref 2). Coating thicknesses were 300-600 μm.

Freestanding samples (1×1 cm^2) of the as-sprayed B_4C were fabricated by dissolving the titanium alloy substrate using nitric acid. As-sprayed B_4C specimens were cross sectioned with a diamond saw, cold epoxy mounted under low pressure, and fine polished using No. 800 SiC paper followed by 9, 3, and 1 μm diamond suspensions and then an 0.05 μm alumina suspension to minimize the pullout of particles.

Surface hardness measurements were conducted using both Vickers and Knoop indenters in a Zwick (Ulm, Germany) microhardness machine under applied loads of both 3 and 5 kgf for the Vickers indenter and 500 gf for the Knoop indenter. Nanoindentation experiments were performed using a Shimadzu Dynamic Ultra-micro Hardness tester (M/S Shimadzu Co., Japan) equipped with a Berkovich diamond indenter. The tests were performed by loading to the maximum load (from 30 to 190 mN), holding for 20 s, and then complete unloading. Five indents were made at each load on each specimen.

A Nikon Measurescope-11 was used for optical microscopy and a Hitachi S-4500 (Tokyo, Japan) for scanning electron microscopy (SEM) of polished and fracture surfaces of the speci-

mens. The electron energy loss spectroscopy (EELS) was performed using a dedicated scanning transmission electron microscope (STEM, JEOL 2010F) (Tokyo, Japan) that was operated at 200 kV. This field emission microscope is equipped with a Gatan Imaging Filter, model US1000FT 3 (Gatan Inc., Pleasanton, CA). The STEM unit is driven by Gatan Digiscan software to acquire EELS spectra and images. Sections of the as-sprayed B_4C parallel to the substrate were prepared for transmission electron microscopy (TEM) by mechanical polishing followed by ion beam milling to electron transparency.

X-ray diffraction (XRD) was performed on a Siemens D5000 Diffractometer System (Siemens, Madison, WI), using Cu-K_α radiation operating at 50 kV/35 mA over an angular range of $15° < 2\theta < 95°$ for both the initial powder and the as-sprayed structure. The total carbon content of the initial powder and as-sprayed material was measured using the carrier hot gas extraction method (LECO). Characterization of the initial powder and the as-sprayed B_4C sample was also performed using a microRaman spectrometer with the incident laser beam focused to a spot size of about 40 μm in diameter. Surfaces of the powder and as-deposited specimens were analyzed by x-ray photoelectron spectroscopy (XPS) using a PHI 5500 ESCA system (Physical Electronics, Chanhassen, MN). The XPS spectra were generated by a Mg-K_α source with photon energy of 1253.6 eV. The spectra from the as-deposited specimens were recorded at a photoelectron takeoff angle of 45°. To minimize surface effects, the initial powder sample was tilted to 75° instead of 45°. The analyzed area was approximately 1 mm^2 within 12 nm of the surface after sputtering by an Ar^+ ion beam of 3 keV energy. The peak positions were aligned and corrected for charge effects based on the adventitious C*1S* peak position at 284.8 eV.

3. Results and Discussion

3.1 Mechanical Properties

Hardness measurements were carried out using both Knoop and Vickers indenters. Knoop hardness tests were performed with the long axis of the Knoop indenter both parallel and perpendicular to the splat spread direction. The applied load for Knoop hardness measurements was 500 gf. The as-sprayed B_4C has an average hardness of 1236 ± 140 KH parallel to the splats and 1583 ± 103 KH in the perpendicular orientation. Some cracks along the splat boundaries oriented in the direction of the large diagonal of the Knoop indenter can be observed (Fig. 1).

Hardness measurements with the Vickers indenter were performed using both 5 and 3 kgf loads. The average hardness was in the range of 950 ± 50 and 1033 ± 200 HV for 5 and 3 kgf loads, respectively. Similar variations in the hardness values were reported in previous studies. The hardness values were slightly higher than those reported for samples deposited using an APS process (Ref 1, 2, 4, 6).

Nanoindentation experiments were performed using a range of loads, from 30 to 190 mN. The measured maximum indentation depth and plastic deformation depth are given in Table 1. The optical micrograph in Fig. 2 shows the position of the indentations listed in Table 1. It is worth noting that after unloading, from 30 to 50% (depending on the applied load and position) of the total depth remains as a residual (plastic) deformation (Fig. 3). The range of the nanohardness values was from

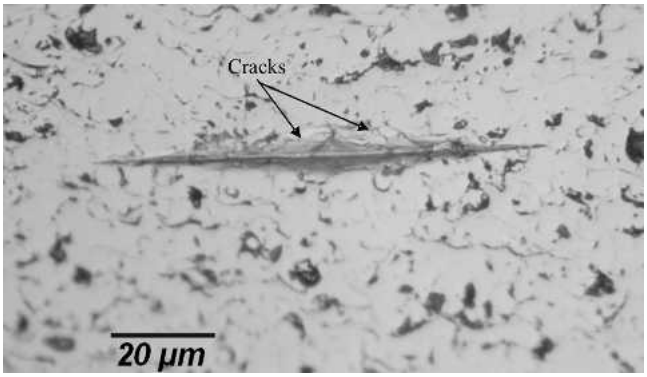

Fig. 1 Micrograph of VPS B_4C showing cracks propagation all around the indentation area

Table 1 Measured nanohardness results

Load	Position	Maximum depth, nm	Plastic depth, nm	Nanohardness, GPa
190 mN	1	920	427	43
	2	668	490	33
	3	860	421	44
	4	902	400	39
150 mN	1	762	373	44
	2	785	410	37
	3	783	403	38
	4	692	316	61
	5	706	338	54
100 mN	1	585	284	51
	2	618	325	39
	3	653	362	31
	4	736	470	19
	5	634	308	31
50 mN	1	379	206	48
	2	384	206	48
	3	383	200	51
	4	380	210	46
	5	382	189	57
30 mN	1	292	178	39
	2	300	176	39
	3	262	110	101
	4	275	116	91
	5	261	110	100
	6	145	130	73
	7	268	150	54

19 to 100 GPa, which reflects the inhomogeneity in the structure. The measured nanohardness values are slightly higher than those reported by Han et al. (Ref 1) for B_4C films deposited with the magnetron sputtering method. The factors responsible for the low level and wide variation in the measured hardness values are explored in the following sections.

3.2 Phase Analyses

The diffraction patterns of the as-sprayed B_4C and the initial powder are shown in Fig. 4. The x-ray patterns indicate that the main phase is B_4C with broadened peaks. The amount of boron nitride is reduced significantly in the as-sprayed structure compared with the initial powder. There are two amorphous

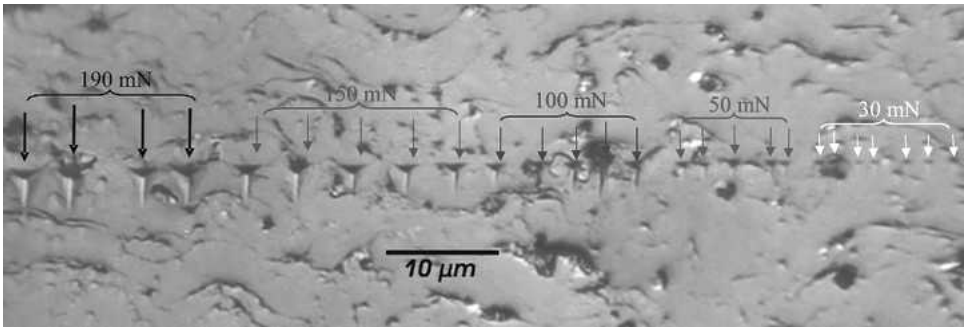

Fig. 2 Optical micrograph of VPS B_4C showing nanohardness indentations

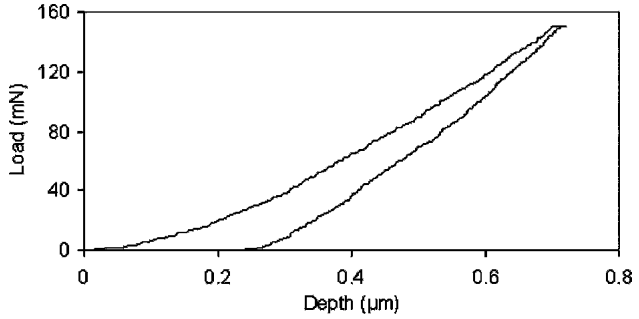

Fig. 3 Load versus indenter displacement curve of VPS B_4C

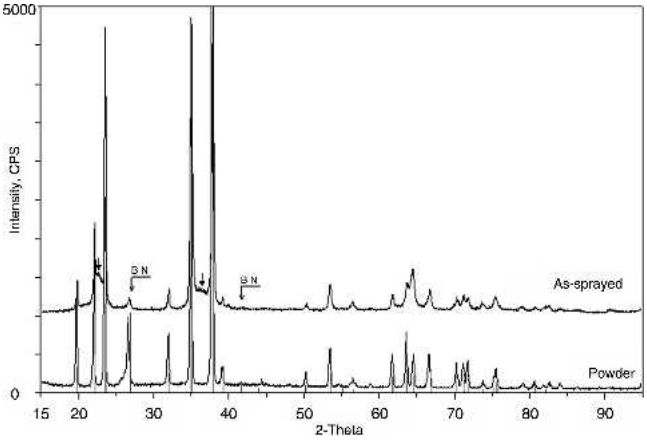

Fig. 4 XRD patterns of initial powder and as-sprayed B_4C. Arrows indicate the amorphous phase in the as-sprayed structure.

"humps" on the trace of the as-sprayed sample, marked by the arrows in Fig. 4. They both occur between pairs of the strongest B_4C peaks and could be caused by an amorphous material having a short-range order close to the interatomic distance in the B_4C structure. These humps most likely indicate the presence of an amorphous nonstoichiometric B_4C ($B_{4-x}C$) phase in the material as reported previously by Zeng et al. (Ref 4) for B_4C deposited on stainless steel using an APS system.

The Raman spectra obtained from the as-sprayed specimen and initial powder show a series of Raman bands extending from 200 to 2000 cm^{-1} (Fig. 5). A broad signal ranging from 1200 to

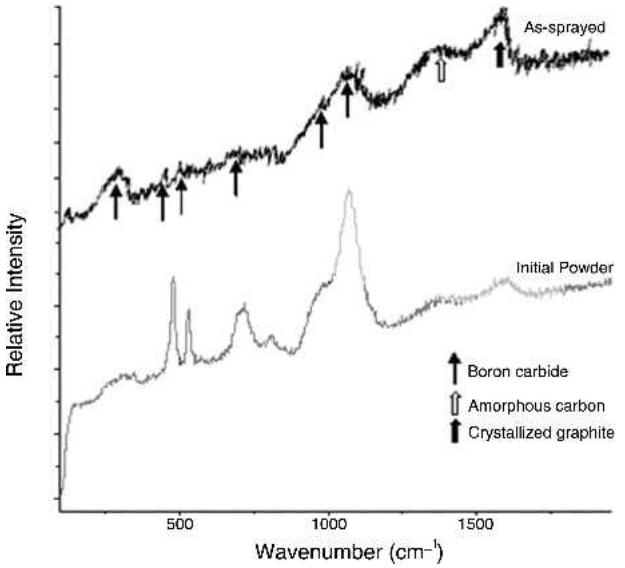

Fig. 5 Raman spectrum from the polished surface of the VPS B_4C and initial powder. Arrows indicate crystalline B_4C, crystalline graphite, and amorphous carbon.

2000 cm^{-1} can be observed. It appears to include two bands: the ~1550 cm^{-1} peak, which is the only peak for crystalline graphite, and the ~1375 cm^{-1} peak, which is assigned to amorphous carbon (Ref 7). Raman bands at ~330, ~475, ~530, and ~1120 cm^{-1} associated with B_4C can also be seen in the spectra. The spectrum of the initial powder reveals sharper peaks for B_4C than those of as-sprayed structures, indicating that the as-sprayed material is more highly stressed and less well crystallized. The as-sprayed material has a higher level of free carbon in the forms of crystalline graphite and amorphous carbon than the initial powder.

3.3 Composition Analyses

The bulk carbon content measured by LECO for both B_4C powder and as-sprayed specimens was 20.7 wt.%. Thus there is no significant change in the total carbon content in the as-sprayed specimen compared with the initial powder. Stoichiometric B_4C would be 18.3 wt.% carbon. Assuming all boron is present as B_4C, approximately 1.4 wt.% of the carbon atoms

would exist as free carbon corresponding to 2.9 wt.% free carbon in the sample. This is consistent with the Raman spectra, which show the presence of crystalline graphite and amorphous carbon. At this level, it is unlikely that the crystalline graphite would be seen in the XRD pattern.

The surface chemistry of the as-sprayed B_4C and the initial powder was investigated using XPS analysis. Figure 6(a-1) shows the typical XPS spectra of B*1S* core-level electrons from VPS B_4C. The B*1S* peak was fit with three different peaks centered at 187.8, 189.5, and 191.6 eV, suggesting that the boron atoms in the coatings are in different bonding configurations. The major fraction of the boron atoms is present as B_4C. The lower binding energy of the B*1S* peak at 187.8 eV is attributable to electrons originating from boron atoms bonded to carbon in B_4C. The higher binding energy of the B*1S* peak at 189.5 eV can be assigned to nonstoichiometric B_4C ($B_{4-x}C$). The small peak at 191.6 eV can be attributed to B-O bonding (Ref 5, 8, 9).

The typical spectra of C*1S* core-level electrons is shown in Fig. 6(a-2). The XPS spectrum reveals that the carbon atoms are involved in several types of chemical bonding. Three individual peaks can be deconvoluted from the fitted C*1S* peak, centered at 282.5, 284.4, and 286.2 eV. The major fraction of carbon atoms is present as amorphous carbon at a bonding energy of 284.4 eV in the sprayed structure. The energy peak at 282.5 eV is identified as originating from the B_4C phase. The bonding energy at 286.2 likely corresponds to C-O bonds (Ref 5, 8).

Both B*1S* and C*1S* spectra from the initial B_4C powder are shown in Fig. 6(b) for comparison. Deconvolution for the B*1S* spectra would suggest two peaks corresponding to two different chemical states for boron atoms. As for the VPS materials, the

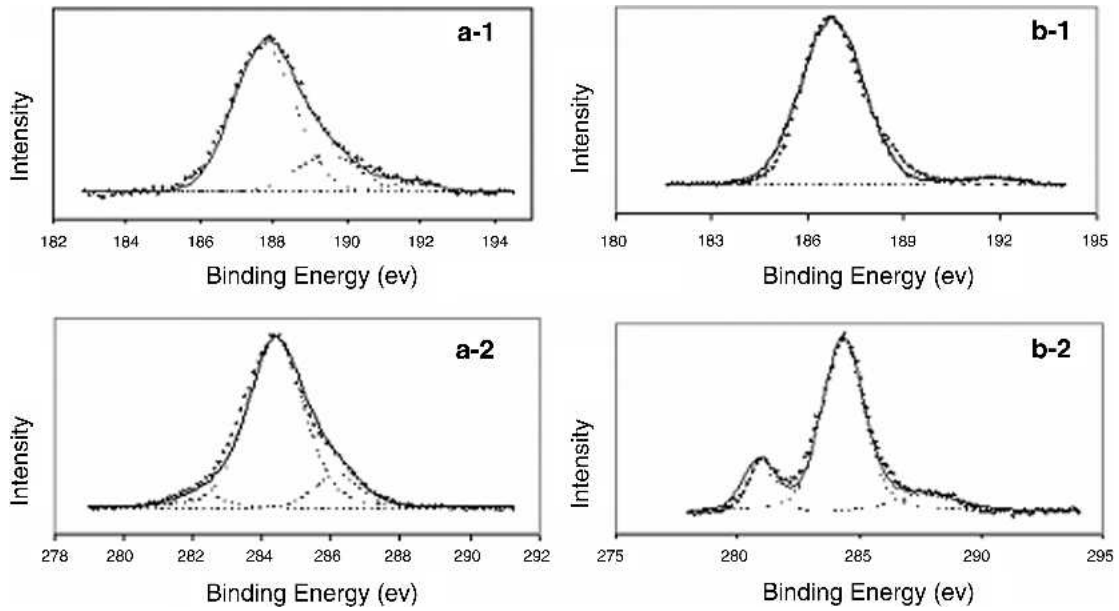

Fig. 6 XPS spectrum of (a) VPS B_4C and (b) initial powder of B_4C; a-1 and b-1: B*1S*; a-2 and b-2: C*1S*

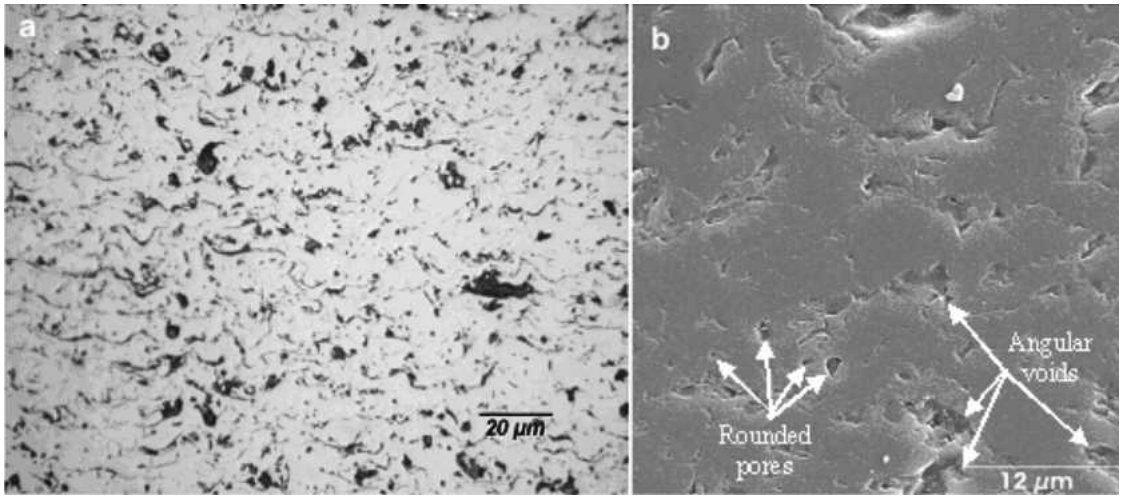

Fig. 7 Micrographs of the polished cross section of the VPS B_4C, (a) optical image and (b) SEM image

main contribution to the B*1S* spectra centered at 186.7 eV is attributed to boron atoms to carbon, and the small peak at 191.6 eV can be assigned to B-O bonding (Ref 5, 8, 9). In contrast to the B*1S* spectra from the as-sprayed structure, nonstoichiometric $B_{4-x}C$ is not evident in the initial powder. The C*1S* spectrum of the initial powder can be fit with three peaks as shown in Fig. 6(b-2). As for the VPS material, the main contribution, centered at 284.4 eV, is attributed to the presence of amorphous carbon in the structure. The lower binding energy peak centered at 281.2 eV is identified as originating from C-B bonding (B_4C phase), whereas a small peak centered at 288 eV is attributed to C-O binding energy (Ref 10). Hence, the intensity of the C-O peak increases in the as-sprayed structure compared with the initial powder because of the oxidation of B_4C droplets and deposited splats during spraying. Moreover, the intensity of the amorphous carbon peak in the as-sprayed structure increases compared with the initial powder, indicating the decomposition of B_4C during spraying.

Quantitative analysis of the amount of carbon present as amorphous carbon or graphite is difficult. The values estimated from the peak height ratio in the XPS spectra are ~70% of total carbon for the initial powder and ~80% for the as-deposited material. Similar estimations from the Raman spectra suggest that ~20% of total carbon in the powder and ~60% in the as-deposited material exists as amorphous carbon and graphite.

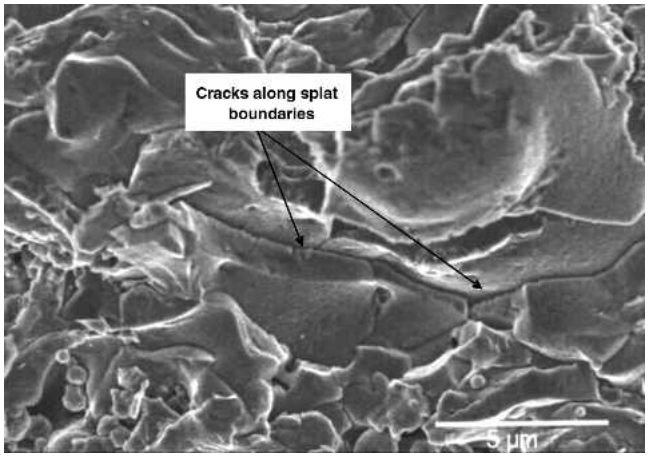

Fig. 8 Fracture surface of the VPS B_4C

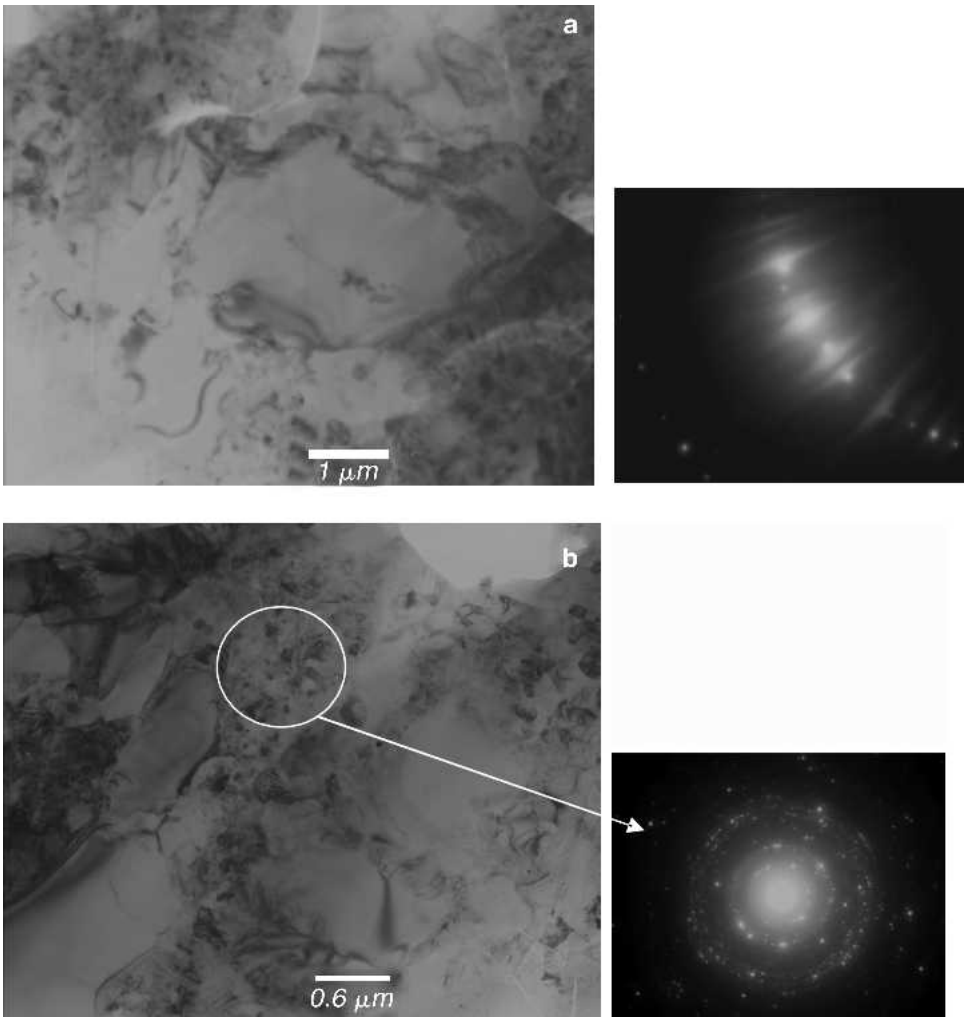

Fig. 9 TEM bright-field image and SAED pattern from (a) large-grain area and (b) nanograin structure of VPS B_4C

These techniques, especially XPS, are highly surface sensitive. Compared with the 1-2% of free carbon estimated from LECO results, which is a bulk analysis, it must be concluded that the free carbon is found almost exclusively at the surface of the powder particles and at the surface and internal interfaces of the deposit.

3.4 Microstructure Analyses

The microstructure of a cross section of the VPS B_4C is shown in Fig. 7. The splat structure is clearly observed. The polished cross section indicates that the majority of the particles were molten at impact and have spread to produce apparently good contact between the individual particles. Two types of apparent pore can be seen. The first type is larger, rounded pores between the splats caused by gas entrapment during deposition. The second type is characterized by angular edges, which suggest that they are the result of the loss of solid particles or fragments. Bianchi et al. (Ref 3) suggested that these types of angular particle may have been formed by the residual stresses resulting from the high cooling rate of splats on impact, which would lead to the curling of splat edges and therefore poor cohesion along the rim of the splat. These rim areas could then be broken and possibly ejected from the coating by the impact of subsequent splats.

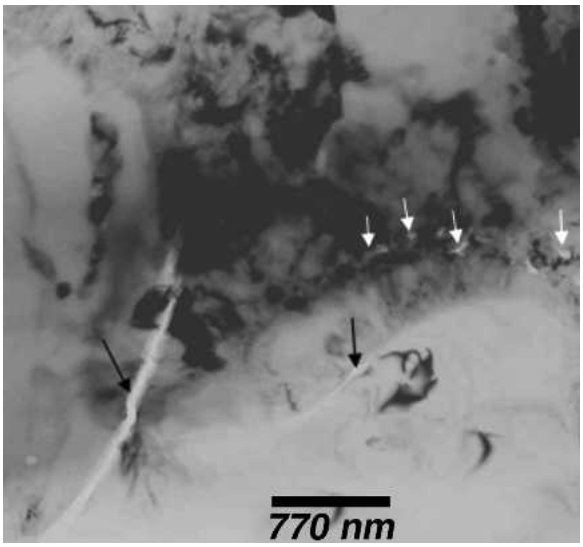

Fig. 10 TEM bright-field image of VPS B_4C. White arrows indicate small pores caused by gas entrapping, and black arrows show cracks along splat boundaries.

Fracture surfaces of as-sprayed specimens (Fig. 8) reveal lamellae structure with a high density of unmelted and partially melted particles. The thickness of splats ranges from 1 to 4 μm and the diameter from 10 to 50 μm. A high density of cracks along splat boundaries can be seen, indicating low cohesion between the splats.

TEM observations from a section parallel to the substrate of an as-sprayed specimen revealed an equiaxed grain structure (Fig. 9). The grain size ranged from 300 nm to 3 μm. A mixture of amorphous and microcrystalline phases can also be observed. TEM bright-field images and selected-area electron diffraction (SAED) patterns from both large B_4C grains and fine-crystallite areas are also shown in Fig. 9. The SAED pattern from the fine-crystallite area exhibits diffuse rings indicative of amorphous or microcrystalline structures, while the SAED pattern from a large B_4C grain shows single-crystal features.

Fine pores, 100-300 nm in diameter, can be seen in the microstructure, as shown by the white arrows in the TEM micrograph of a section parallel to the substrate in Fig. 10. These are located within the fine-scale structure between the large B_4C grains. Microcracks (black arrows) located between particles or splats can also be seen. Such microcracks are the result of a high level of local stress caused by the rapid solidification and the low toughness of B_4C (Ref 3).

A STEM micrograph of a particle or grain boundary is shown in Fig. 11. The crevice formed in the boundary is caused by preferential thinning, suggesting the presence of a softer phase at the boundary. To quantify the carbon concentration, spectra were taken from several raster areas of a known size (40 × 5 nm) on both the particle and boundary. The spectrum shown in Fig. 12(a) is typical of those collected from the interior of the grain, with a B:C peak height ratio of approximately 1.9. Spec-

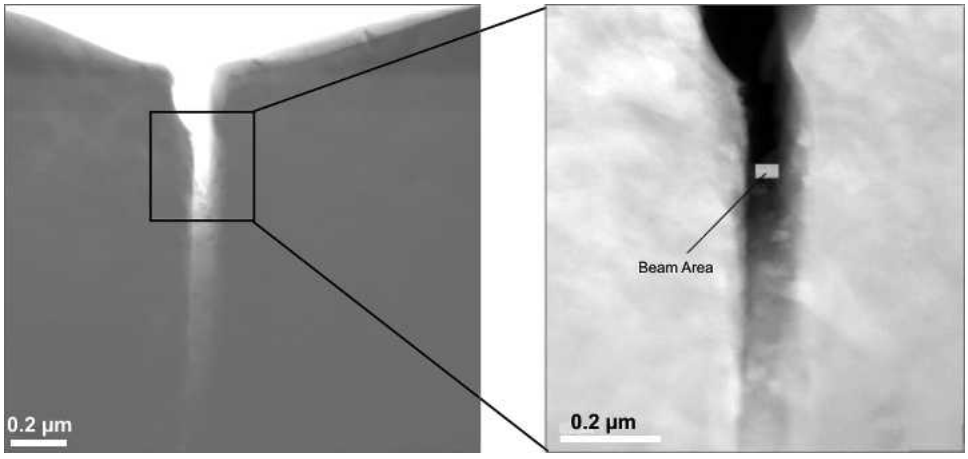

Fig. 11 STEM image of a particle or grain boundary in B_4C. The beam is focused into the boundary (right).

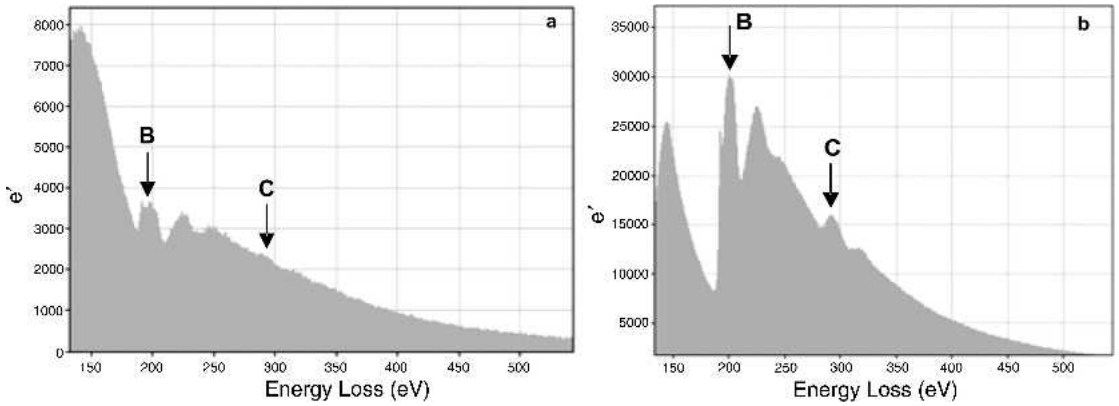

Fig. 12 EELS spectrum obtained from a 40 × 5 nm area covering (a) grain and (b) boundary

tra taken from the crevice at the boundary show an increased in concentration of carbon, with a peak height ratio of 1.5. Depletion of boron at the boundary is consistent with the existence of free carbon on the surface of the initial powder particles as observed by XPS and the conclusion drawn from comparison of the XPS, Raman, and LECO analyses.

4. Conclusions

In this study, B_4C was deposited successfully on Ti-6Al-4V alloy using the VPS process. The deposited structure contains B_4C, nonstoichiometric $B_{4-x}C$, crystalline and amorphous graphite, and a small amount of B_2O_3. The amount of nonstoichiometric $B_{4-x}C$, graphite, and oxide increased in the as-sprayed structure compared with the initial powders of B_4C because of decomposition of B_4C during spraying. A high level of carbon at the surface and boundaries and concurrent boron depletion are consistent with the existence of free carbon on the surface of the initial powder as well as decomposition of B_4C through volatilization of boron during spraying. The presence of a soft phase at grain and splat boundaries resulting from the decomposition of B_4C and the existence of pores and microcracks along particle and splat boundaries result in the lower hardness of the as-sprayed structure relative to bulk B_4C. The Vickers hardness was 1033 ± 200 HV for a 3 kgf load. The range in hardness values is the result of the inhomogeneous structure containing porosity, nonstoichiometric $B_{4-x}C$, and free carbon phases at grain boundaries and splat boundaries in the as-sprayed structure.

Acknowledgments

The financial support for this work was provided by the Natural Science and Engineering Research Council of Canada and PyroGenesis, Inc. The authors thank Dr. L. Persian and Dr. D. Grozea for technical assistance and acknowledge Dr. Dr. G. Botton and F. Pearson at Brockhouse Institute for Materials Research at McMaster University for STEM and EELS analyses.

References

1. Z. Han, G. Li, J. Tian, and M. Cu, Microstructure and Mechanical Properties of Boron Carbide Thin Films, *Mater. Lett.,* Vol 57, 2002, p 899-903
2. A. Cavasin, T. Brzeinski, S. Grenier, M. Smagorinski, and P. Tsantrizos, W and B_4C Coatings for Nuclear Fusion Reactors, *Thermal Spray: Meeting the Challenges of the 21st Century,* C. Coddet, Ed., May 25-29, 1998 (Nice, France), ASM International, 1998, p 957-961
3. L. Bianchi, P. Brelivet, A. Freslon, and C. Cordillot, Plasma-Sprayed Boron Carbide Coatings as First Wall Material for Laser Fusion Target Chamber, *Thermal Spray: Meeting the Challenges of the 21st Century,* C. Coddet, Ed., May 25-29, 1998 (Nice, France), ASM International, 1998, p 945-950
4. Y. Zeng, S.W. Lee, and C. Ding, Study on Plasma-Sprayed Boron Carbide Coating, *J. Thermal Spray Technol.,* Vol 11 (No. 1), 2002, p 129-133
5. Y. Zeng, C. Ding, and S. Lee, Young's Modulus and Residual Stress of Plasma-Sprayed Boron Carbide Coatings, *J. Eur. Ceram. Soc.,* Vol 21, 2001, p 87-91
6. J.E. Doring, R. Vaben, J. Linke, and D. Stover, Properties of Plasma-Sprayed Boron Carbide Protective Coatings for the First Wall in Fusion Experiments, *J. Nuclear Mater.,* Vol 307-311 (No. 1), 2002, p 121-125
7. V. Domnich, Y. Gogotsi, M. Trenary, and T. Tanaka, Nanoindentation and Raman Spectroscopy Studies of Boron Carbide Single Crystals, *Appl. Phys. Lett.,* Vol 81 (No. 20), 2002, p 3783-3785
8. H. Ling, J.D. Wu, J. Sun, W. Shi, Z.F. Ying, and F.M. Li, Electron Cyclotron Resonance Plasma-Assisted Pulsed Laser Deposition of Boron Carbide Nitride Films, *Diamond Relat. Mater.,* Vol 11, 2002, p 1623-1628
9. G.I. Kalandadze, S.O. Shalamberidze, and A.B. Peikrishvili, Sintering of Boron and Boron Carbide, *J. Solid State Chem.,* Vol 154, 2000, p 194-198
10. A.O. Sezer and J.I. Brand, Chemical Vapor Deposition of Boron Carbide, *Mater. Sci. Eng.,* Vol B79, 2001, p 191-202